PHYSICAL REVIEW B **108**, 214304 (2023)

Strong four-phonon effects and anomalous thermal transport behavior in the monolayer group-IVB transition metal dichalcogenides MX_2 (M=Ti, Zr, Hf; X = S, Se)

Zhunyun Tang,[1,*] Xiaoxia Wang,[1,*] Jin Li,[1] Chaoyu He,[1] Mingxing Chen,[2] Chao Tang,[1,†] and Tao Ouyang[1,‡]
[1] *School of Physics and Optoelectronics and Hunan Key Laboratory for Micro-Nano Energy Materials and Device, Xiangtan University, Xiangtan 411105, Hunan, China*
[2] *College of Physics and Information Science, Hunan Normal University, Changsha, 410081, China*

(Received 14 July 2023; revised 20 September 2023; accepted 27 November 2023; published 7 December 2023)

The discovery of strong four-phonon (4ph) interactions in boron arsenide has spurred significant investigations into the influence of higher-order phonon anharmonic scattering on the thermal transport of materials. Considering the special relative regular residual feature and great potential applications in thermoelectrics, this study systematically investigates the anharmonic lattice dynamics and thermal transport behavior of monolayer group-IVB transition metal dichalcogenides 1T-MX_2 (M = Ti, Zr, Hf; X = S, Se) via *ab initio* calculations with the self-consistent phonon and Boltzmann transport theories. The calculation results indicate that 1T-MX_2 has strong 4ph anharmonic scattering and that the phonon dispersion exhibits a significant temperature dependence, which stems from the obvious in-plane quartic potential well vibrations of the transition metal atoms. When 4ph scattering is considered, a remarkable reduction of thermal conductivity is observed in 1T-MX_2, especially for 1T-TiS_2 and 1T-$TiSe_2$, with their conductivity reduction reaching 66 and 62% at room temperature, respectively. Moreover, the thermal conductivity of 1T-MX_2 anomalously increases when the M atoms transition from Ti → Zr → Hf, which is in contrast to the traditional intuitive impression where heavy atomic systems always exhibit poor thermal transport performance. Such abnormal mass-dependent behavior of thermal conductivity mainly arises from the enhancement of the bond energy (reduction of phonon anharmonicity) in the Zr and Hf systems. The study results shed light on the physical mechanism of the thermal transport in monolayer 1T-MX_2 and provides helpful insights into the necessity of considering the influence of 4ph effects on thermal transport.

DOI: 10.1103/PhysRevB.108.214304

I. INTRODUCTION

Lattice thermal conductivity (κ_L), a fundamental physical property of materials, plays a critical role in various technical and engineering applications, e.g., micro- and nanodevices, thermoelectric energy transformation, and high-efficiency thermal management devices [1–4]. To satisfy the different requirements of thermal transport performance in these fields, materials with suitable thermal conductivity need to be identified (e.g., low thermal conductivity for thermoelectric and thermal barrier devices and high thermal conductivity for heat dissipation devices). Among the numerous factors affecting thermal conductivity, phonon anharmonic scattering is an important factor. In the past decades, researchers mainly focused on the anharmonic scattering of materials based on the three-phonon (3ph) theory, while largely overlooking the more intricate four-phonon (4ph) scattering. This is because in most materials, 4ph scattering is often a perturbation of the 3ph scattering; consequently, reasonably accurate results can be obtained by considering only the third-order term [5–7]. However, the 4ph effect cannot be ignored in some materials. For instance, the materials tend to have certain atoms with highly spatial symmetry, or certain phonon modes that exhibit significant imaginary frequency U-shaped pocket at 0 K. Recently, Feng *et al.* observed anomalously strong 4ph scattering in boron arsenide (BAs) crystals, wherein the predicted room-temperature thermal conductivity decreased from 2200 to 1400 W/mK (approximately 33% reduction) when 4ph scattering was considered [8,9]. Subsequent experimental studies also observed the same phenomenon and determined that the measured value of the room-temperature thermal conductivity of BAs ranges from ∼1000 to ∼ 1300 W/mK [10–12]. The theoretical calculations considering the 4ph effect align more closely with the experimental results than the calculations not considering the 4ph effect, implying that the 4ph effect plays a crucial role in the BAs crystals. In addition to BAs, strong 4ph anharmonic effects have been observed in other bulk materials [13–28], such as perovskite, antiperovskite, and full Heusler compounds.

The harmonic approximation (HA) phonon theory is a common method for obtaining phonon information in the ground state (0 K). However, it cannot accurately describe the thermal transport properties of certain materials, especially for systems that are dynamically unstable at 0 K or whose phonon dispersion exhibits significant temperature-dependent behavior. To overcome such limitations, the self-consistent phonon (SCP) theory [29,30] is proposed, which is an approach for including anharmonic effects beyond the perturbation theory, considering the quantum effect of phonons. Specifically, the

---

[*] These authors contributed equally to this work.
[†] tang_chao@xtu.edu.cn
[‡] ouyangtao@xtu.edu.cn

Hamiltonian within the HA ($H = T + U$) contains only the quadratic term of potential energy, whereas the SCP theory introduces higher-order terms and yields the anharmonic renormalization phonon frequencies. Therefore, both higher-order phonon scattering (3ph and 4ph) and the SCP theory are important for correctly evaluating the thermal transport properties of these materials.

Two-dimensional (2D) materials have recently attracted great interest because of their fascinating electronic, optical, thermal, and mechanical properties [31–34]. Typical 2D materials can be classified into superflat hexagonal honeycomb structures (graphene, *h*-BN, etc.) [35,36], pentagonal structures (pentagraphene, penta-CN_2, etc.) [37,38], transition metal carbides and carbonitrides (*MX*enes; e.g., $Ti_3C_2T_X$, Ti_3CN, etc.) [39,40], and transition metal dichalcogenides (TMDs; e.g., MoS_2, $ZrSe_2$, etc.) [41,42]. Owing to their unique properties, including high carrier mobility, large thermoelectric figure of merit, and ease of fabrication, TMDs have recently attracted considerable attention [43–52]. Among the TMDs compounds, 1*T*-MX_2 (M = Ti, Zr, Hf; X = S, Se) possesses better prospects for thermoelectric applications than 2H-MX_2 (M = Mo, W; X = S, Se), primarily due to the lower κ_L. However, the previous studies on the thermal conductivity of 1*T*-MX_2 are not consistent, and obvious differences in the thermal conductivity of the same material have been reported by different research groups. For example, Ding *et al.*, Xiang *et al.*, and Chen *et al.* determined the room-temperature thermal conductivity of 1*T*-$HfSe_2$ to be 1.8, 5.54, and 26 W/mK, respectively [47,51,52]. Such significant differences could stem from an inadequate understanding of the phonon properties. Furthermore, 1*T*-TiS_2 and 1*T*-$TiSe_2$ exhibit a special charge-density wave behavior (negative phonon frequencies) at low temperatures [53–59], implying that the solution of the phonon Boltzmann equation within HA is invalid. Moreover, in our preliminary research works, the transition metal atoms M in 1*T*-MX_2 (M = Ti, Zr, Hf; X = S, Se) are observed to exhibit an unusually significant quartic potential-energy well model of in-plane vibrations. Such a feature suggests that quite strong 4ph anharmonic effects could be present in these monolayer structures. Consequently, the inclusion of anharmonic phonon renormalization and four-order anharmonic scattering is essential for correctly determining the physical picture of the phonon aspects for 1*T*-MX_2.

Motivated by the above statements, this study systematically investigates the anharmonic lattice dynamics and thermal transport behavior of 1*T*-MX_2 monolayers (M = Ti, Zr, Hf; X = S, Se) using *ab initio* calculations combined with the SCP and Boltzmann transport theories. The calculation results show that 1*T*-MX_2 possesses strong 4ph anharmonic scattering and that the phonon dispersion exhibits significant temperature dependence, arising from the obvious in-plane quartic potential well vibrations of the transition metal atoms M. Additionally, the thermal transport properties are severely influenced by these particular behaviors. Within the framework of the SCP theory, for example, the introduction of 4ph scattering could cause a remarkable reduction of the thermal conductivity of 1*T*-TiS_2 (1*T*-$TiSe_2$) from 3.82 (2.55) to 0.82 (0.61) W/mK at 900 K, and the reduction magnitude could be as high as 79% (76%). Moreover, thermal conductivity anomalously increases with the mass of the M atoms in these structures. The underlying physical mechanism of this unique phenomenon is determined by analyzing the bond features. The remainder of the paper is organized as follows. In the next section, the calculation details are briefly described. In Sec. III, detailed analyses of the chemical bonding, temperature-dependent phonon dispersion, κ_L, group velocity, phonon scattering, phase space, and Grüneisen parameters are presented to reveal the phonon-related mechanisms in 1*T*-MX_2. Finally, the conclusions are summarized in Sec. IV.

II. COMPUTATIONAL METHODOLOGY

In this study, the first-principles calculations are implemented in the Vienna *Ab initio* Simulation Package (VASP) [60]. The Perdew-Burke-Ernzerhof (PBE) generalized function of generalized gradient approximation is used as the exchange-correlation potential [61], and the reliability of the obtained results is proven from various aspects [see Table SI, Fig. S1, and Fig. S2 in the Supplemental Material (SM) [62]; see also Refs. [53,59,63–65] therein]. The wave functions are expanded in plane-wave basis with the kinetic energy cutoff of 500 eV, and the *k* mesh of 15 × 15 × 1 is used to sample the Brillouin zone, with the energy convergence threshold set as 10^{-8} eV. A large vacuum region of 15Å is set to prevent the interactions between the monolayer and its mirrors induced by the periodic boundary conditions. The lattice constants and coordinates of all the atoms are fully optimized until the maximum residual stress is less than 10^{-4} eV/Å. The HA second-order interatomic force constants (second IFCs) and phonon dispersion are obtained using the ALAMODE package [29,66] via the finite displacement approach (0.01 Å) with a supercell of 5 × 5 × 1, where the *k* mesh of 3 × 3 × 1 is used. Compressive sensing lattice dynamics (CSLD) [67–69], which is a method that incorporates machine learning to realize accelerated and accurate capture of higher-order IFCs, is used to obtain the third- and fourth-order anharmonic IFCs (third and fourth IFCs). Specifically, a 5000-step *ab initio* molecular dynamics (AIMD) simulation is performed at 300 K with a 4 × 4 × 1 supercell. The AIMD simulations are performed using 1-fs time step and *NVT* ensemble. Then, 80 snapshot structures are sampled by skipping the first 1000 steps in the trajectories, with a frequency of 50 steps. Subsequently, to reduce the correlation between these atomic structures, every atom of the 80 snapshots is displaced by 0.1 Å in a random direction. Finally, accurate static

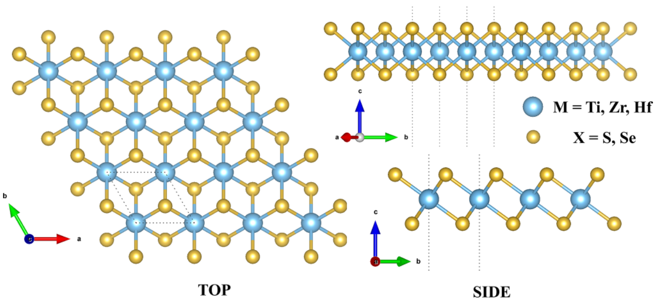

FIG. 1. Lattice structure of the top and side views of 1T-MX_2 (M = Ti, Zr, Hf; X = S, Se) monolayers.

TABLE I. Calculated $a(b)^{\rm cal}$ for the lattice parameter of the 1T-MX_2 (M = Ti, Zr, Hf; X = S, Se) monolayers. $|\gamma|^{\rm HA}$ and $|\gamma|^{\rm SCP}$ represent the Grüneisen parameters obtained from the HA and SCP theories, respectively. P_3 and P_4 denote 3ph and 4ph scattering phase spaces, respectively. The other work $a(b)^{\rm cal}$ and the experimental lattice constants $a(b)^{\rm exp}$ are listed for comparison.

	$a(b)^{\rm cal}$ (Å) (this work)	$a(b)^{\rm cal}$ (Å) (other work)	$a(b)^{\rm exp}$ (Å)	$\|\gamma\|^{\rm HA}$	$\|\gamma\|^{\rm SCP}$	$P_3^{\rm HA}$ (10^{-3})	$P_3^{\rm SCP}$ (10^{-3})	$P_4^{\rm HA}$(10^{-3})	$P_4^{\rm SCP}$(10^{-3})
$\mathrm{TiS_2}$	3.40	3.42 [44]	–	–	2.49	–	4.73	–	4.47
$\mathrm{TiSe_2}$	3.52	3.52 [45]	3.54 [63]	–	2.38	–	7.48	–	5.96
$\mathrm{ZrS_2}$	3.68	3.68 [46]	–	2.20	2.05	5.95	5.84	5.03	5.03
$\mathrm{ZrSe_2}$	3.80	3.80 [48]	–	2.36	2.14	8.16	7.59	7.28	7.22
$\mathrm{HfS_2}$	3.64	3.64 [51]	–	2.06	1.94	6.44	5.75	5.16	5.19
$\mathrm{HfSe_2}$	3.75	3.76 [52]	–	2.12	1.85	8.79	8.07	7.74	7.77

density-functional theory calculations are performed using a 3 × 3 × 1 k mesh to obtain the corresponding displacement and force datasets, and fitting is performed by the least absolute shrinkage and selection operator technique to obtain the third and fourth IFCs. Thereafter, using the iterative (3ph mode information) and relaxation time approximation (4ph mode information) solution method implemented in FOURPHONON software [70,71], the $\kappa_{\rm L}$ and phonon mode-level information are calculated by solving the phonon Boltzmann transport equation:

$$\kappa_{\rm L}^{\alpha\beta} = \frac{1}{k_b T^2 V N}\sum_{\lambda} n_0(n_0+1)(\hbar\omega_\lambda)^2 v_\lambda^\alpha F_\lambda^\beta, \tag{1}$$

$$F_\lambda^\beta = \tau_\lambda^0\left(v_\lambda^\beta + \Delta_\lambda\right), \tag{2}$$

where λ is the phonon-mode index containing both the phonon branch and wave vector. Additionally, k_b, V, N, and $\hbar$ are the Boltzmann constant, volume, wave-vector number, and reduced Planck's constant, respectively. α and β are the Cartesian directions. τ_λ^0 represents the phonon relaxation time, v_λ^β denotes the phonon group velocity, and Δ_λ represents the correction term. Taking 1T-ZrSe$_2$ as an example, the convergence of $\kappa_{\rm L}$ is rigorously analyzed and the results are provided in Fig. S3 in the SM [62]. To balance the computational cost and accuracy, a phonon q grid of 41 × 41 × 1 and a scalebroad of 0.5 (0.2) are used to compute the convergent three (four)-phonon information. Furthermore, the seventh and fourth nearest-neighbor atoms are used as interaction cutoffs for the third and fourth IFCs, respectively. The effective thickness of 7.0 Å is used to correct the thermal conductivity values yielded by the FOURPHONON code. Moreover, a comparison is performed between the thermal conductivity values obtained from higher-order force constants calculated using the pure first principles (conventional finite displacement approach) and those obtained through the CSLD technique. No significant differences are observed between the results of the two methods, but the former consumes nearly two orders of magnitude more than the latter in the acquisition of the force constants. Subsequently, the CSLD technique is used to calculate the higher-order force constants for the other five structures in 1T-MX_2 (M = Ti, Zr, Hf; X = S, Se). As shown in Figs. S4 and S5 in the SM [62], the LO-TO splitting weakly influences the thermal conductivity. The differences in thermal conductivity between the case with and without the LO-TO splitting are all below 7%. Therefore, the LO-TO splitting is not considered throughout the $\kappa_{\rm L}$ investigation.

The SCP calculation is performed to obtain the temperature-dependent phonon dispersion using the HA

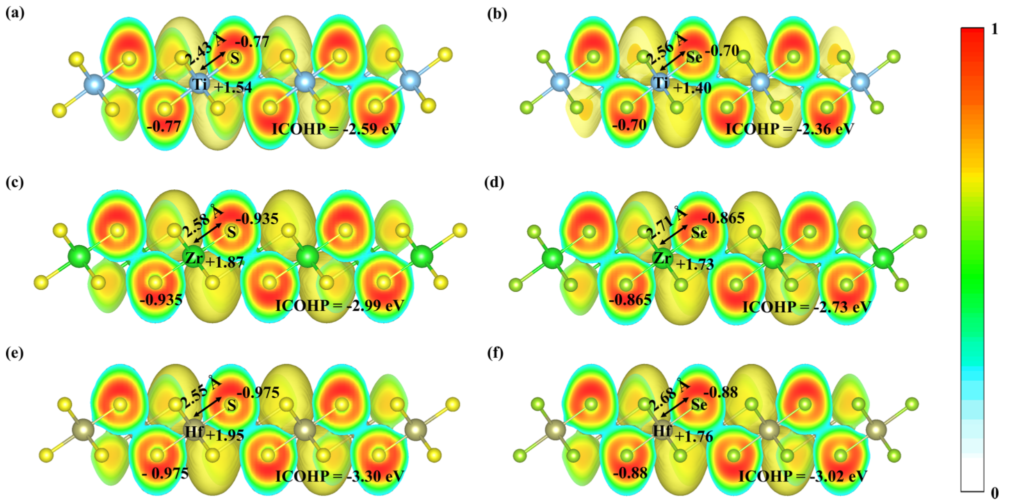

FIG. 2. Isosurfaces of the ELF of 1T-MX_2 (M = Ti, Zr, Hf; X = S, Se) monolayers. The lengths and ICOHP of the different chemical bonds as well as the Bader effective charges of the different atoms are labeled.

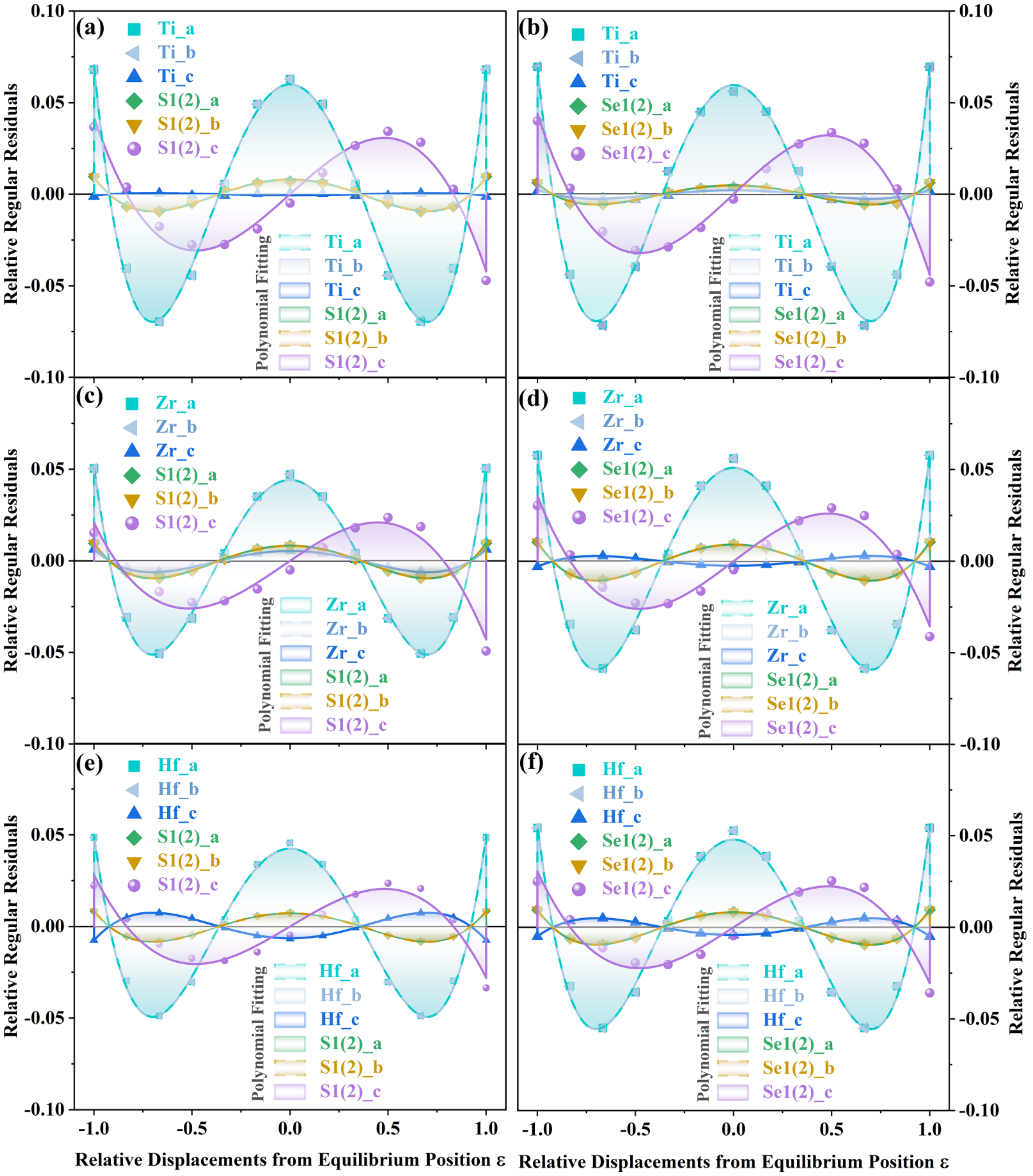

FIG. 3. Calculated RRR curves for non-equivalent atoms in different directions of (a) 1T-TiS_2, (b) 1T-$TiSe_2$, (c) 1T-ZrS_2, (d) 1T-$ZrSe_2$, (e) 1T-HfS_2, and (f) 1T-$HfSe_2$ monolayers.

second- and higher-order IFCs. The temperature-dependent anharmonic phonon frequencies can be solved using the following equation:

$$\Omega_\lambda^2 = \omega_\lambda^2 + 2\Omega_\lambda I_\lambda, \tag{3}$$

$$I_\lambda = \sum_{\lambda_1} \frac{\hbar\Phi(\lambda; -\lambda; \lambda_1; -\lambda_1)}{8\Omega_\lambda \Omega_{\lambda_1}}[2n(\Omega_{\lambda_1}) + 1], \tag{4}$$

where ω_λ, Ω_λ, and $\Phi(\lambda; -\lambda; \lambda_1; -\lambda_1)$ are the harmonic phonon frequencies, temperature-dependent anharmonic phonon frequencies, and fourth IFCs, respectively. More details about the SCP theory can be found in a previous study [29,30].

III. RESULTS AND DISCUSSION

The MX_2 (M = Ti, Zr, Hf; X = S, Se) materials belong to the 1T-phase TMDs with space group P-3m1 (No. 164). Owing to the weak van der Waals interactions between the layers, 1T-MX_2 2D films or monolayers have been successfully prepared in recent experiments [42,63,72–77]. As shown in Fig. 1, the 1T-MX_2 monolayers contain three atomic sublayers, with the M atomic layer sandwiched between two X atomic layers. Additionally, the M atoms are combined with six neighboring X atoms and act as an inversion center for the X atoms. Table I presents the sufficiently optimized lattice constants. Due to the intrinsic symmetry of 1T-MX_2 (i.e., a- and b-lattice direction is isotropic), $a = b$. The results of this study well agree with those of previous theoretical and experimental works [44–46,48,51,52,63]. The bond lengths (L) are marked in Fig. 2, and they align with the trend observed in the lattice constants. With the exception of a slight decrease in the bond length of $\langle \text{Hf–}X \rangle$ ($L_{\langle \text{Hf–}X \rangle}$) compared to that of $\langle \text{Zr–}X \rangle$ ($L_{\langle \text{Zr–}X \rangle}$), the remaining bond lengths increase with the mass of the bonding atoms. Generally, according to the Badger rule [78,79], larger bond lengths correspond to weaker

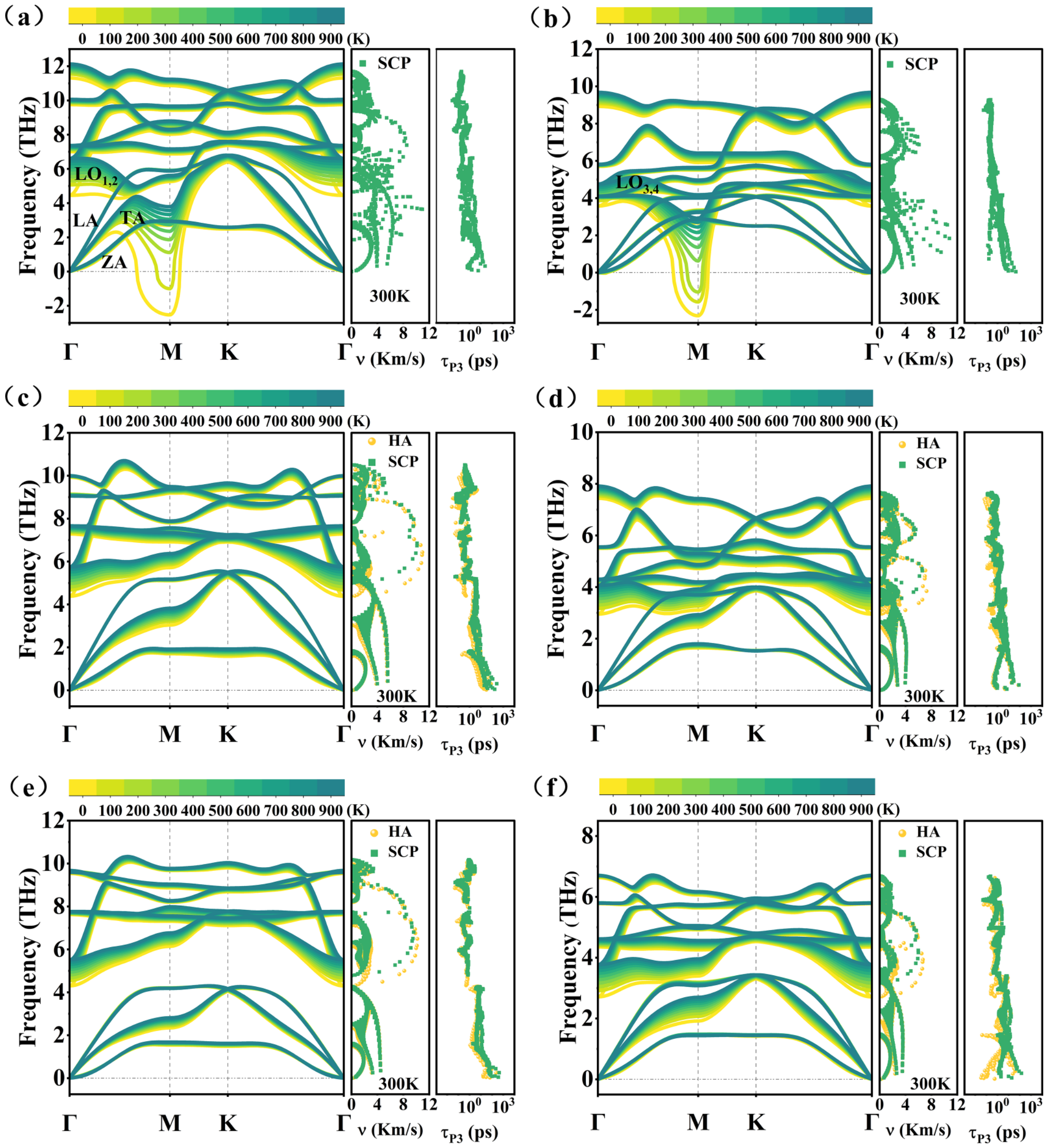

FIG. 4. Calculated phonon dispersion curves, group velocity (ν), and relaxation time (τ) of (a) 1T-TiS$_2$, (b) 1T-TiSe$_2$, (c) 1T-ZrS$_2$, (d) 1T-ZrSe$_2$, (e) 1T-HfS$_2$, and (f) 1T-HfSe$_2$. Left panel: Harmonic (T = 0 K) and anharmonic (T = 100 ∼ 900 K) phonon dispersion curves calculated based on the SCP theory. Middle and right panels: The values of ν and τ (only 3ph scattering is considered) at 300 K obtained through the HA or SCP theory.

bond strengths (*Str*), and such behavior has been demonstrated in most materials [80–82]. To quantitatively analyze the bond strength of different $\langle M\text{–}X\rangle$ in 1T-MX_2, the integrated crystal orbital Hamilton population (ICOHP) is calculated. ICOHP is calculated from the wave-function file in VASP using the LOBSTER package [83], and the higher the negative value of ICOHP, the stronger the bond strength. As depicted in Fig. 2, $\langle M\text{–Se}\rangle$ has a larger bond length and a smaller negative ICOHP value than $\langle M\text{–S}\rangle$ when sulfide atoms (X) are used as the single variable, obeying the Badger rule. However, surprisingly, when the transition metal atom (M) is used as the single variable, the bond strengths of $\langle \text{Ti–}X\rangle$, $\langle \text{Zr–}X\rangle$, and $\langle \text{Hf–}X\rangle$ are not negatively correlated with the bond length. Specifically, $Str_{\langle Ti\text{–}X\rangle} < Str_{\langle Zr\text{–}X\rangle} < Str_{\langle Hf\text{–}X\rangle}$, i.e., the bond strength increases with the mass of M atoms, which is in contrast to the Badger rule. To understand these phenomena, the electron localization function (ELF) is calculated and Bader charge analysis is performed on 1T-MX_2. Figure 2 shows that electrons are mainly localized on the sulfide group atoms X, forming strong polar bonds. Additionally, the Bader charge denotes the specific value of the charge transfer from the M atoms to the X atoms (where "+" represents the contributing charge and "−" represents the receiving charge). The more charges transferred between two bonding atoms, the stronger the bonding energy and electronegativity. Among the six materials considered, $\langle \text{Hf–S}\rangle$ exhibits the strongest electronegativity, while $\langle \text{Ti–Se}\rangle$ exhibits the weakest electronegativity, which is consistent with the ICOHP description of the bond strength. As is well known, heavy atoms tend to suppress the group velocity of a system, and the weak bonding

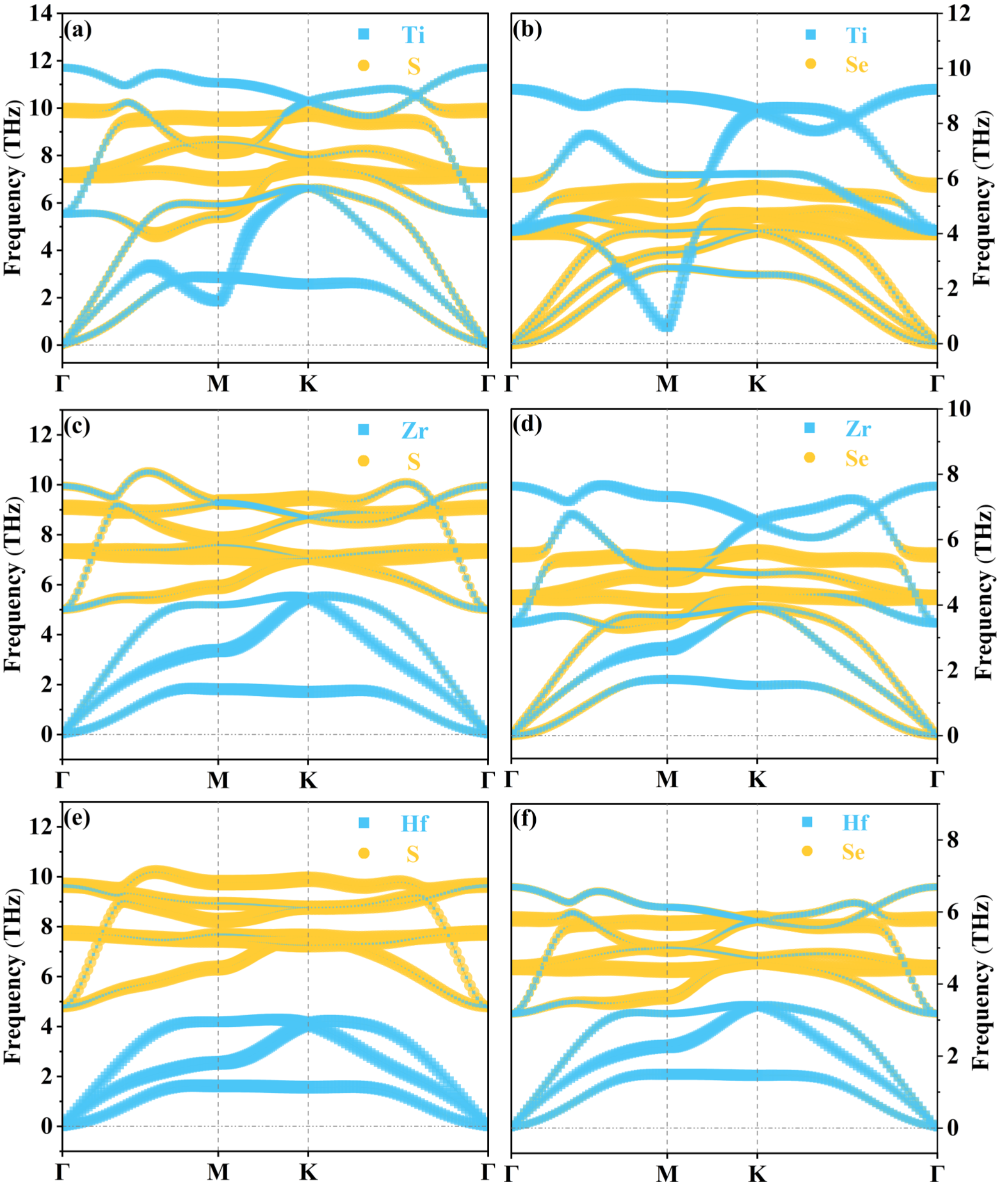

FIG. 5. Calculated atomic projection phonon dispersion curves at 300 K for (a) 1T-TiS$_2$, (b) 1T-TiSe$_2$, (c) 1T-ZrS$_2$, (d) 1T-ZrSe$_2$, (e) 1T-HfS$_2$, and (f) 1T-HfSe$_2$.

stemming from the heavy atoms always tends to simultaneously enhance the anharmonic scattering. Such synergistic effects of the group velocity and anharmonic scattering can severely suppress the thermal transport of heavier systems. Therefore, previous studies commonly employed the heavy average atomic mass as the criteria for high-throughput exploration of materials with intrinsically low κ_L [84–89]. In 1T-MX_2 (M = Ti, Zr, Hf; X = S, Se), nevertheless, the bond strength increases with the atomic mass from Ti → Zr → Hf. This unusual phenomenon suggests that the two key factors affecting thermal conductivity, i.e., anharmonic scattering and group velocity, may exhibit competing rather than synergistic behavior in 1T-MX_2.

To further evaluate the anharmonicity of 1T-MX_2 (M = Ti, Zr, Hf; X = S, Se), atomic perturbations are performed along different directions and energy versus displacement profiles are derived, and then, the deviations from the HA are quantified to obtain the corresponding relative regular residuals (RRR) [34,90,91]. Interestingly, these systems exhibit unusually strong 4ph anharmonicity. When the anharmonicity is primarily driven by 4ph interactions, RRR exhibits a “W” or “M” shape. Otherwise, RRR exhibits a “∽” or “∼” shape. As illustrated in Fig. 3, the transition metal atoms M exhibit very strong 4ph anharmonicity along the in-plane vibrations (i.e., a- and b-lattice direction), which is greater than the 3ph anharmonicity exhibited by the sulfide group atoms X along the out-of-plane vibrations (c-lattice direction). Such a phenomenon implies that when calculating the thermal conductivity of 1T-MX_2, the contribution of 4ph interactions cannot be overlooked. Moreover, the difference in RRR values between S and Se atoms is not significant. However, RRR noticeably decreases as the atoms change from Ti → Zr → Hf, indicating a weakening of the anharmonicity within the corresponding systems, which is consistent with the

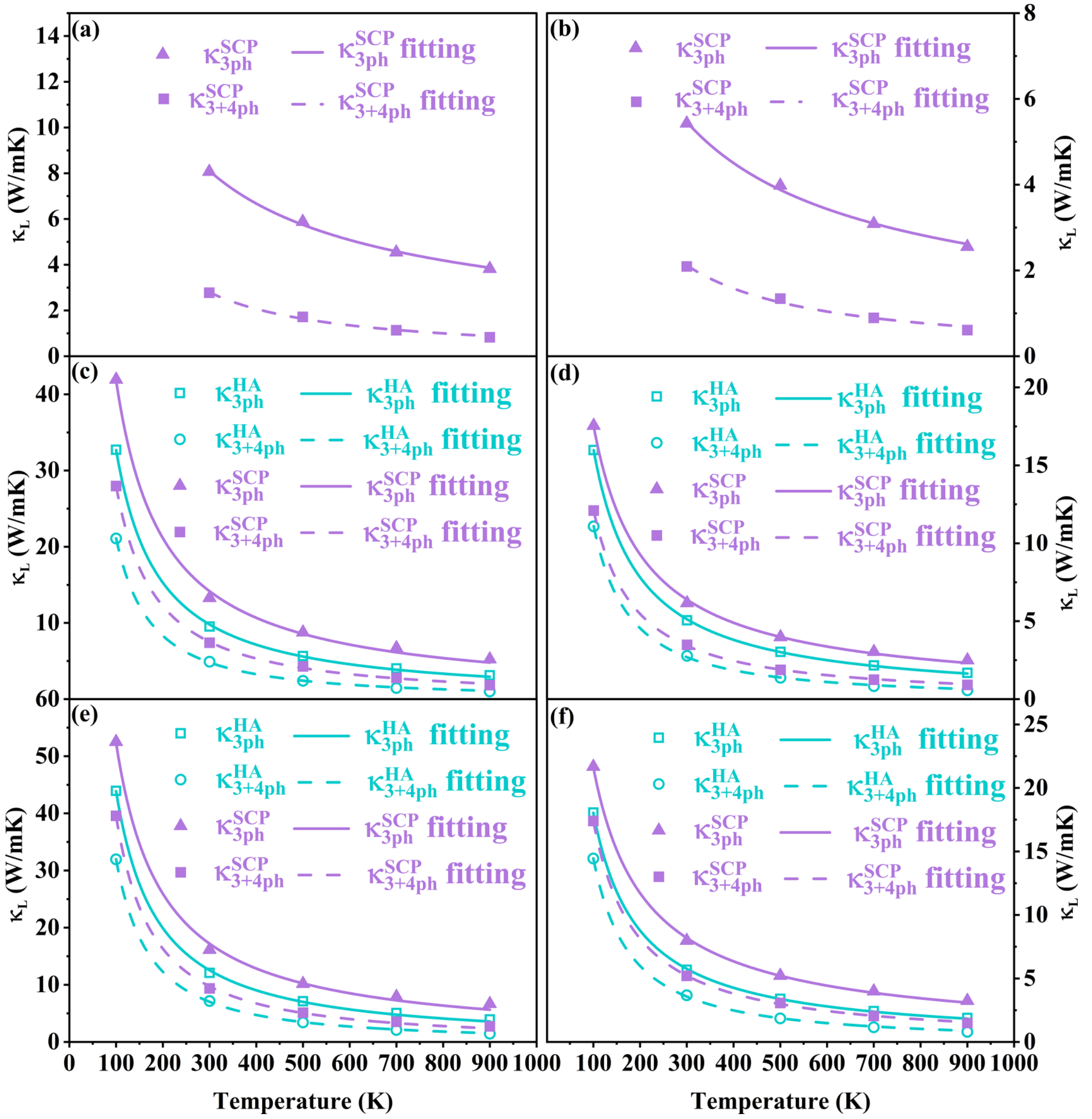

FIG. 6. Thermal conductivity calculated with different models as a function of temperature for (a) 1T-TiS$_2$, (b) 1T-TiSe$_2$, (c) 1T-ZrS$_2$, (d) 1T-ZrSe$_2$, (e) 1T-HfS$_2$, and (f) 1T-HfSe$_2$.

anharmonic behavior reflected by the bond strength analysis shown in Fig. 2. Notably, to illustrate that the 3ph anharmonicity in 1*T*-*MX*$_2$ is not weak, the Grüneisen parameter and RRR of 1*T*-*MX*$_2$ and 1*T*-SnS$_2$ are compared. 1*T*-SnS$_2$ is the system exhibiting strong 3ph anharmonicity, as demonstrated in several previous studies [64,65]. The results show (Figs. S6–S8 in the SM [62]) that the Grüneisen parameter magnitude and the third-order RRR (" ∼ " or " ∼ ") of 1*T*-*MX*$_2$ are comparable to those of 1*T*-SnS$_2$, where 1*T*-Ti*X*$_2$ is even slightly larger than 1*T*-SnS$_2$. This implies that 1*T*-*MX*$_2$ also possesses strong 3ph anharmonicity. Figure S8 intuitively shows that the fourth-order RRR (*W* or *M*) of 1*T*-SnS$_2$ are not significant, which is quite different from those of 1*T*-*MX*$_2$ (Fig. S7). Such results further demonstrate the strong 4ph anharmonicity in 1*T*-*MX*$_2$.

The renormalized phonon frequencies may be significantly influenced by the potentially strong 4ph anharmonicity. As shown in Fig. 4, the phonon spectrum curves of 1*T*-*MX*$_2$ exhibit obvious temperature-dependent behavior. Specifically, the phonon dispersion of 1*T*-*MX*$_2$ significantly increases with the temperature, especially for the transverse acoustic (TA) phonon mode at the high-symmetry point *M* and the lowest two optical (LO$_{12}$) phonon modes [the lowest third and fourth optical (LO_{34}) phonon modes for 1*T*-TiSe$_2$] at the high-symmetry point Γ. Moreover, Figs. 5(a) and 5(b) display the 1*T*-TiS$_2$ and 1*T*-TiSe$_2$ host imaginary phonon frequencies within HA (0 K), indicating that lattice instability occurs at 0 K. The instability of 1*T*-TiS$_2$ and 1*T*-TiSe$_2$ at low temperatures stems from their special charge-density wave behavior, as verified in previous experimental and theoretical works [53–59]. To distinguish the atomic contribution of these special phonon modes, the atomic projection phonon dispersion of 1*T*-*MX*$_2$ at 300 K is plotted in Fig. 5, and the figure shows that the transition metal atoms *M* mainly contribute to these modes. This implies that the strong 4ph anharmonicity in 1*T*-*MX*$_2$ is dominated by the transition metal atoms *M*.

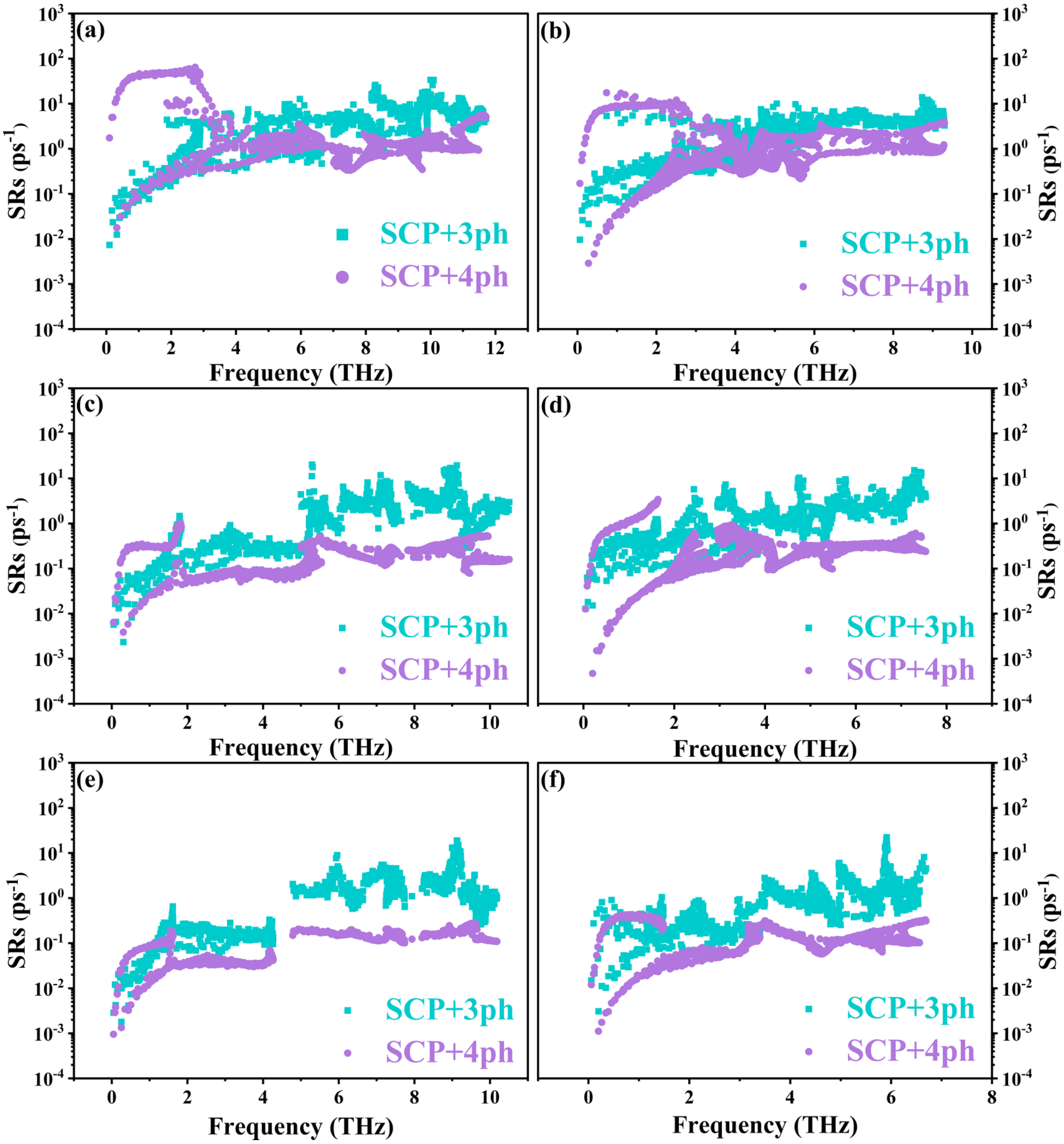

FIG. 7. Comparison of 3ph and 4ph SRs based on SCP theory for (a) 1T-TiS$_2$, (b) 1T-TiSe$_2$, (c) 1T-ZrS$_2$, (d) 1T-ZrSe$_2$, (e) 1T-HfS$_2$, and (f) 1T-HfSe$_2$.

Figure 6 depicts the κ_L values of 1*T*-*MX*$_2$ obtained using different models. In the HA theory, the κ_L obtained considering only 3ph interactions is denoted as κ_{3ph}^{HA}, and that obtained also considering the 4ph interactions on the base of 3ph is denoted as κ_{3+4ph}^{HA}. Similarly, after phonon renormalization using the SCP theory, i.e., replacement of the HA phonon frequency ω_λ with the renormalized frequency Ω_λ in Eq. (1), the corresponding κ_L is denoted as κ_{3ph}^{HA} and κ_{3+4ph}^{SCP}, respectively. Since 1*T*-TiS$_2$ and 1*T*-TiSe$_2$ have imaginary HA phonon frequencies, the solution of the phonon Boltzmann transport equation is not valid for these materials. Therefore, only κ_{3ph}^{SCP} and κ_{3+4ph}^{SCP} are provided in Figs. 6(a) and 6(b). In Figs. 6(c)–6(f), the κ_L calculated using the SCP theory is significantly larger than that using the HA theory. To elucidate this phenomenon, the group velocities (ν) and relaxation times (τ) of the four materials (1*T*-ZrS$_2$, 1*T*-ZrSe$_2$, 1*T*-HfS$_2$, and 1*T*-HfSe$_2$) at different approximations (HA and SCP) are determined and illustrated in the right panel of Fig. 4. Here, the 3ph model at 300 K is taken as an example. The anharmonic renormalization significantly increases the slope of the TA phonon mode along the Γ–*M* path, which increases the ν of TA mode in the low-frequency region. Conversely, the LO$_1$ mode gradually levels off with increasing temperature on the Γ–*K* path, resulting in the decrease of ν. Consequently, the total ν magnitude remains relatively unchanged, denoting that the influence of ν on the thermal conductivity can be neglected. However, τ increases overall, implying that the phonon anharmonic scattering rates (τ^{-1}) decrease and play a positive role in the enhancement of the thermal conductivity of 1*T*-*MX*$_2$ under SCP approximations. The combined analysis of ν and τ indicates that the latter is the key factor influencing the thermal conductivity increase in the SCP model. Moreover, Table I lists the Grüneisen parameter (γ) and scattering phase space (P_3), which are two key factors affecting the

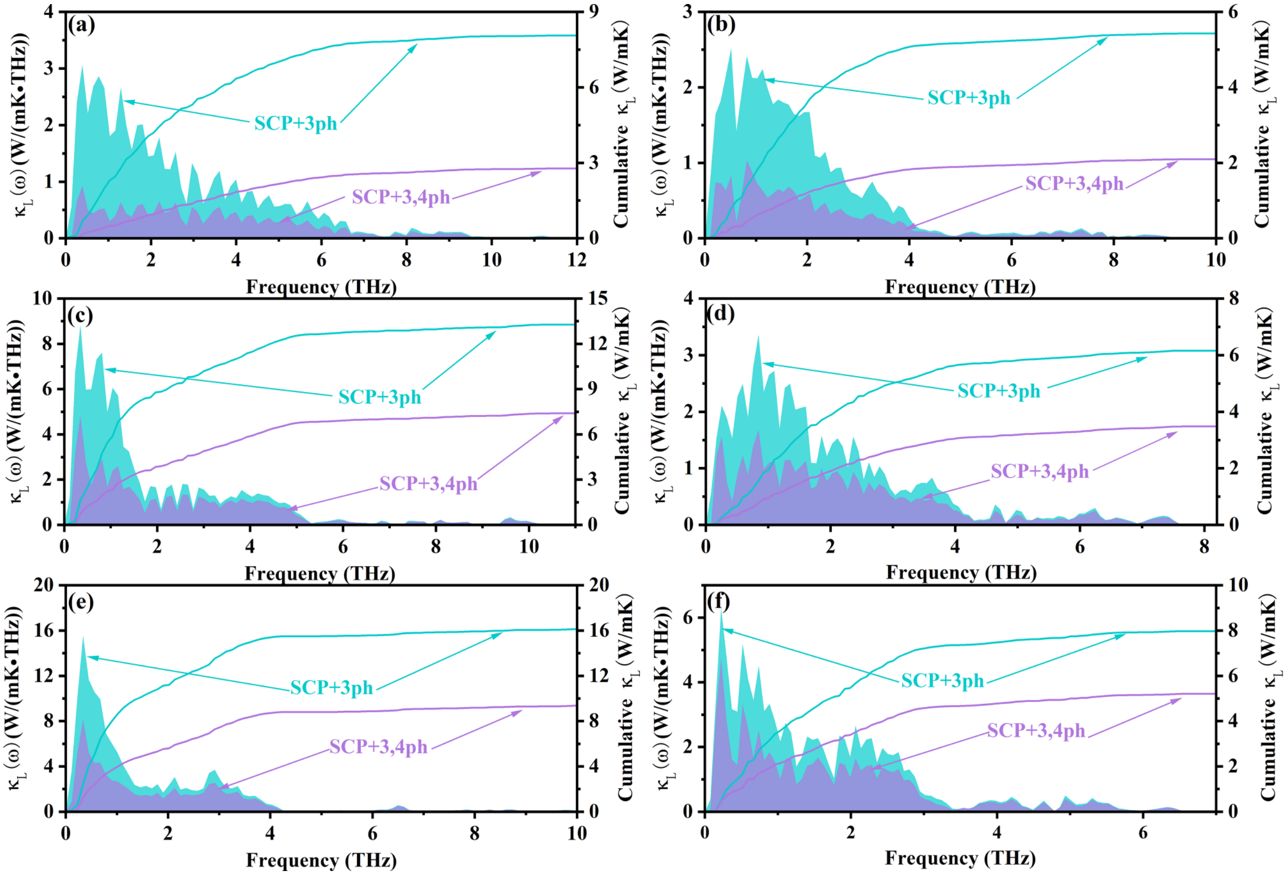

FIG. 8. Thermal conductivity spectra $\kappa_L(\omega)$ calculated within the SCP + 3ph and SCP + 3,4ph models at 300 K for (a) 1T-TiS$_2$, (b) 1T-TiSe$_2$, (c) 1T-ZrS$_2$, (d) 1T-ZrSe$_2$, (e) 1T-HfS$_2$, and (f) 1T-HfSe$_2$.

anharmonic scattering. Larger $|\gamma|$ (anharmonic scattering intensity) and P_3 (anharmonic scattering possibility) signify stronger anharmonic scattering. As shown in Table I, $|\gamma|^{\mathrm{SCP}} < |\gamma|^{\mathrm{HA}}$ and $P_3^{\mathrm{SCP}} < P_3^{\mathrm{HA}}$, further revealing the underlying physical mechanism of the SCP scattering rate reduction in 1*T*-*MX*$_2$. Notably, $|\gamma|$ represents the average value of each mode γ after taking absolute values.

Since the SCP theory is more reliable for obtaining the real phonon physical picture, $\kappa_{3\mathrm{ph}}^{\mathrm{SCP}}$ and $\kappa_{3+4\mathrm{ph}}^{\mathrm{SCP}}$ are focused on in the subsequent analysis. As shown in Fig. 6, $\kappa_{3\mathrm{ph}}^{\mathrm{HA}}$ and $\kappa_{3+4\mathrm{ph}}^{\mathrm{SCP}}$ decrease with increasing atomic mass of *X* (S, Se) and increase with the atomic mass of *M* (Ti, Zr, and Hf). The latter behavior is an extremely abnormal phenomenon. To further explain the anomalous mass-dependent behavior of thermal conductivity, the ν values and anharmonic scattering rates (SRs) are analyzed. The combination of Figs. 4 and 7 shows that although the thermal transport of the heavy *M*-atoms system is suppressed by the decrease of ν, the positive effect of the decrease of SRs on thermal transport overcomes this negative effect, ultimately leading to an increase in the thermal conductivity. However, Table I shows that the magnitude of the scattering phase space (P_3 and P_4) increases as the *M* atoms transition from Ti → Zr → Hf, positively influencing the SRs. This is contradictory to the SRs trend observed in Fig. 7. Consequently, the reduction of the phonon anharmonic intensity in the heavy-atom system is the fundamental reason for the decrease of SRs, and the reduced $|\gamma|^{\mathrm{SCP}}$ and RRR correctly reflect this trend. Note that $|\gamma|^{\mathrm{SCP}}$ reflects the 3ph anharmonic intensity, and to date, no physical parameter similar to $|\gamma|^{\mathrm{SCP}}$ exists that reflects the 4ph anharmonic intensity. Nevertheless, the above-discussed RRR provides a promising direction. In summary, both $|\gamma|^{\mathrm{SCP}}$ and RRR correctly capture the thermal transport behavior in 1*T*-*MX*$_2$ (*M* = Ti, Zr, Hf; *X* = S, Se).

Owing to the strong 4ph anharmonicity of the transition metal atoms (Ti, Zr, and Hf), the thermal transport properties of 1*T*-*MX*$_2$ (*M* = Ti, Zr, Hf; *X* = S, Se) are significantly suppressed. At room temperature, the $\kappa_{3\mathrm{ph}}^{\mathrm{SCP}}$ ($\kappa_{3+4\mathrm{ph}}^{\mathrm{SCP}}$) of 1*T*-TiS$_2$, 1*T*-TiSe$_2$, 1*T*-ZrS$_2$, 1*T*-ZrSe$_2$, 1*T*-HfS$_2$, and 1*T*-HfSe$_2$ is 8.07 (2.77), 5.43 (2.09), 13.27 (7.40), 6.16 (3.48), 16.13 (9.37), and 7.98 (5.20) W/mK, respectively. Upon considering 4ph scattering, the thermal conductivity remarkably decreases in 1*T*-TiS$_2$ and 1*T*-TiSe$_2$ at room temperature, reaching 66 and 62%, respectively. Such suppression of the thermal conductivity is more pronounced for the Ti atomic system due to its stronger 4ph anharmonicity compared to the Zr and Hf atomic systems. Although the percentage reduction in the 1*T*-ZrS$_2$ and 1*T*-Hf*X*$_2$ systems (ranging from 35 to 44%) is lower than that in the 1*T*-Ti*X*$_2$ system, it still exceeds that of some typical strong 4ph anharmonic materials [9,18,20]. Moreover, since 4ph (3ph) scattering is proportional to the temperature T^2 (T) [9], it becomes more important at high temperatures. For instance, the thermal conductivity reduction of 1*T*-TiS$_2$ and 1*T*-TiSe$_2$ at 900 K reaches 79 and 76%, respectively. Figure 7 displays that the 4ph SRs are greater than the 3ph

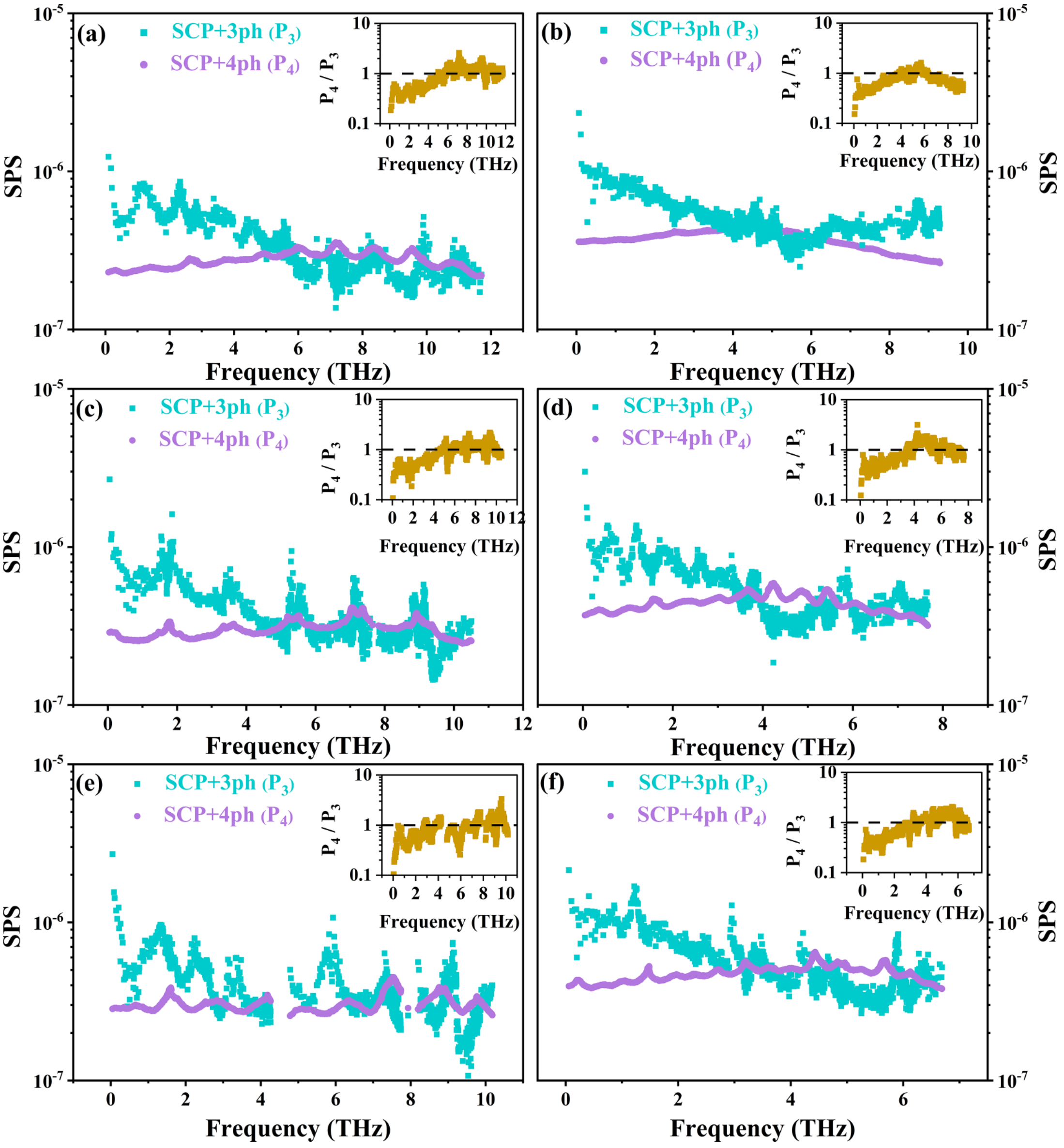

FIG. 9. Comparison of 3ph and 4ph scattering phase space based on SCP theory for (a) 1T-TiS_2, (b) 1T-$TiSe_2$, (c) 1T-ZrS_2, (d) 1T-$ZrSe_2$, (e) 1T-HfS_2, and (f) 1T-$HfSe_2$. Inset: Frequency resolved ratio of the scattering phase space P_4–P_3.

SRs for low-frequency phonons. Therefore, the main reason for the larger decrease in $\kappa_{3+4\text{ph}}^{\text{SCP}}$ compared to that in $\kappa_{3\text{ph}}^{\text{SCP}}$ is the strong 4ph SRs from the low-frequency phonons, and this phenomenon is visually reflected in the thermal conductivity spectra $\kappa_{\text{L}}(\omega)$ in Fig. 8. Interestingly, the strong 4ph SRs of 1*T*-MX_2 cannot be reflected from the standpoint of phonon scattering phase space. As shown in Fig. 9, the 4ph scattering phase space (P_4) in the low-frequency region with strong 4ph SRs is dramatically smaller than the 3ph phase space (P_3). Previous studies have always determined whether to consider the effect of 4ph scattering on the thermal conductivity by comparing the magnitudes of P_3 and P_4: the effect of 4ph can be neglected when P_4 is smaller than P_3 [92,93]. However, this study shows that such a viewpoint is one sided. Even when P_4 is smaller than P_3 in 1*T*-MX_2, it eventually severely suppresses the thermal conductivity due to its strong 4ph anharmonicity.

IV. CONCLUSION

This study systematically investigated the thermal transport properties of group-IVB TMDs 1*T*-MX_2 (M = Ti, Zr, Hf; X = S, Se) monolayers using *ab initio* calculations combined with the SCP and Boltzmann transport theories, which include the effects of the higher-order anharmonic renormalization of phonon frequencies and 4ph scattering.

Specifically, key findings of this study are as follows:

(i) Atomic perturbations were performed along different directions. The results showed that the transition metal atoms M exhibit an unusually significant quartic potential-energy well model of in-plane vibrations. Further residual analysis showed that 1*T*-MX_2 possesses extremely strong 4ph anharmonicity, even stronger than the 3ph anharmonicity.

(ii) In 1*T*-MX_2, the strong 4ph anharmonicity led to a notable temperature-dependent behavior of the phonon dispersion. Among the six materials considered, since 1T-TiS_2 and 1T-TiSe$_2$ possessed imaginary HA phonon frequencies, anharmonic phonon renormalization was more crucial for them to yield a realistic physical picture of the phonon.

(iii) The 4ph SRs of 1T-MX_2 exhibited remarkably large values in the low-frequency phonon modes, even exceeding the 3ph SRs, resulting in the significant suppression of the thermal transport properties. When 4ph scattering was considered, remarkable reduction of the thermal conductivity was observed for 1T-MX_2; particularly, for 1T-TiS_2 and 1T-TiSe$_2$, the conductivity reduction reached 66 and 62% at room temperature, respectively. Surprisingly, the 4ph scattering phase space of 1T-MX_2 was considerably smaller than the 3ph scattering phase space in the low-frequency phonon region, implying that assessing whether a material needs to consider the effect of 4ph on the thermal conductivity through only the scattering phase space is insufficient.

(iv) The thermal conductivity of 1T-MX_2 anomalously increased when the M atoms transitioned from Ti → Zr → Hf, which contradicts the traditional intuitive impression that heavy atomic systems always exhibit poor thermal transport performance. Such anomalous mass-dependent behavior of thermal conductivity is mainly attributed to the enhancement of the bond energy (reduction of phonon anharmonicity) in the Zr and Hf samples.

This study highlights the underlying physical mechanism of thermal transport in 1T-MX_2 and provides helpful insights for the necessity of considering the influence of 4ph effects on the thermal transport of materials.

ACKNOWLEDGMENTS

This work was supported by the Youth Science and Technology Talent Project of Hunan Province (Grant No. 2022RC1197), the National Natural Science Foundation of China (Grants No. 52372260, No. 11974300, and No. 11974299), and the Science Fund for Distinguished Young Scholars of Hunan Province of China (Grant No. 2021JJ10036).

The authors declare no competing interests.

---

[1] N. P. Padture, M. Gell, and E. H. Jordan, Science **296**, 280 (2002).
[2] M. Hu, J. V. Goicochea, B. Michel, and D. Poulikakos, Nano. Lett. **10**, 279 (2010).
[3] G. J. Snyder and E. S. Toberer, Nat. Mater. **7**, 105 (2008).
[4] A. L. Moore and L. Shi, Mater. Today **17**, 163 (2014).
[5] D. A. Broido, M. Malorny, G. Birner, N. Mingo, and D. A. Stewart, Appl. Phys. Lett. **91**, 231922 (2007).
[6] A. Seko, A. Togo, H. Hayashi, K. Tsuda, L. Chaput, and I. Tanaka, Phys. Rev. Lett. **115**, 205901 (2015).
[7] L. Lindsay, D. A. Broido, and T. L. Reinecke, Phys. Rev. Lett. **111**, 025901 (2013).
[8] T. Feng and X. Ruan, Phys. Rev. B **93**, 045202 (2016).
[9] T. Feng, L. Lindsay, and X. Ruan, Phys. Rev. B **96**, 161201(R) (2017).
[10] J. S. Kang, M. Li, H. Wu, H. Nguyen, and Y. Hu, Science **361**, 575 (2018).
[11] S. Li, Q. Zheng, Y. Lv, X. Liu, X. Wang, P. Y. Huang, D. G. Cahill, and B. Lv, Science **361**, 579 (2018).
[12] F. Tian, B. Song, X. Chen, N. K. Ravichandran, Y. Lv, K. Chen, S. Sullivan, J. Kim, Y. Zhou, T.-H. Liu *et al.*, Science **361**, 582 (2018).
[13] Y. Xiao, Y. Zhao, J. Ni, S. Meng, and Z. Dai, Mater. Today Commun. **35**, 105450 (2023).
[14] Y. Zhao, C. Lian, S. Zeng, Z. Dai, S. Meng, and J. Ni, Phys. Rev. B **101**, 184303 (2020).
[15] Z. Liu, X. Yang, B. Zhang, and W. Li, ACS Appl. Mater. Interfaces **13**, 53409 (2021).
[16] L. Xie, J. H. Feng, R. Li, and J. Q. He, Phys. Rev. Lett. **125**, 245901 (2020).
[17] T. Feng, A. O'Hara, and S. T. Pantelides, Nano Energy **75**, 104916 (2020).
[18] Q. Wang, Z. Zeng, and Y. Chen, Phys. Rev. B **104**, 235205 (2021).
[19] Q. Ren, Y. Li, Y. Lun, G. Tang, and J. Hong, Phys. Rev. B **107**, 125206 (2023).
[20] J. Zheng, D. Shi, Y. Yang, C. Lin, H. Huang, R. Guo, and B. Huang, Phys. Rev. B **105**, 224303 (2022).
[21] Y. Zhao, S. Zeng, G. Li, C. Lian, Z. Dai, S. Meng, and J. Ni, Phys. Rev. B **104**, 224304 (2021).
[22] X. Wang, Z. Gao, G. Zhu, J. Ren, L. Hu, J. Sun, X. Ding, Y. Xia, and B. Li, Phys. Rev. B **107**, 214308 (2023).
[23] T. Yue, P. Sui, Y. Zhao, J. Ni, S. Meng, and Z. Dai, Phys. Rev. B **105**, 184304 (2022).
[24] T. Yue, Y. Zhao, J. Ni, S. Meng, and Z. Dai, npj Comput. Mater. **9**, 17 (2023).
[25] Y. Xia, Appl. Phys. Lett. **113**, 073901 (2018).
[26] N. K. Ravichandran and D. Broido, Phys. Rev. B **98**, 085205 (2018).
[27] Y. Xia, V. I. Hegde, K. Pal, X. Hua, D. Gaines, S. Patel, J. He, M. Aykol, and C. Wolverton, Phys. Rev. X **10**, 041029 (2020).
[28] Y. Xia, K. Pal, J. He, V. Ozoliņš, and C. Wolverton, Phys. Rev. Lett. **124**, 065901 (2020).
[29] T. Tadano and S. Tsuneyuki, Phys. Rev. B **92**, 054301 (2015).
[30] T. R. Koehler, Phys. Rev. Lett. **17**, 89 (1966).
[31] K. S. Novoselov, A. K. Geim, S. V. Morozov, D. Jiang, Y. Zhang, S. V. Dubonos, I. V. Grigorieva, and A. A. Firsov, Science **306**, 666 (2004).
[32] S. V. Morozov, K. S. Novoselov, M. I. Katsnelson, F. Schedin, D. C. Elias, J. A. Jaszczak, and A. K. Geim, Phys. Rev. Lett. **100**, 016602 (2008).
[33] G. R. Bhimanapati, Z. Lin, V. Meunier, Y. Jung, J. Cha, S. Das, D. Xiao, Y. Son, M. S. Strano, V. R. Cooper *et al.*, ACS Nano **9**, 11509 (2015).
[34] Z. Tang, X. Wang, J. Li, C. He, M. Chen, X. Li, C. Tang, and T. Ouyang, Appl. Phys. Lett. **123**, 102201 (2023).
[35] A. K. Geim, Science **324**, 1530 (2009).
[36] K. K. Kim, A. Hsu, X. Jia, S. M. Kim, Y. Shi, M. Hofmann, D. Nezich, J. F. Rodriguez-Nieva, M. Dresselhaus, T. Palacios, and J. Kong, Nano Lett. **12**, 161 (2012).
[37] S. Zhang, J. Zhou, Q. Wang, X. Chen, Y. Kawazoe, and P. Jena, Proc. Natl. Acad. Sci. USA **112**, 2372 (2015).

[38] S. Zhang, J. Zhou, Q. Wang, and P. Jena, J. Phys. Chem. C **120**, 3993 (2016).

[39] B. Akuzum, K. Maleski, B. Anasori, P. Lelyukh, N. J. Alvarez, E. C. Kumbur, and Y. Gogotsi, ACS Nano **12**, 2685 (2018).

[40] M. Naguib, V. N. Mochalin, M. W. Barsoum, and Y. Gogotsi, Adv. Mater. **26**, 992 (2014).

[41] A. Splendiani, L. Sun, Y. Zhang, T. Li, J. Kim, C.-Y. Chim, G. Galli, and F. Wang, Nano Lett. **10**, 1271 (2010).

[42] M. J. Mleczko, C. Zhang, H. R. Lee, H.-H. Kuo, B. Magyari-Köpe, R. G. Moore, Z.-X. Shen, I. R. Fisher, Y. Nishi, and E. Pop, Sci. Adv. **3**, e1700481 (2017).

[43] X. Gu and R. Yang, Appl. Phys. Lett. **105**, 131903 (2014).

[44] G. Li, K. Yao, and G. Gao, Nanotechnology **29**, 015204 (2018).

[45] Z.-L. Wang, G. Chen, X. Zhang, and D. Tang, Phys. Chem. Chem. Phys. **23**, 1627 (2021).

[46] H. Y. Lv, W. J. Lu, D. F. Shao, H. Y. Lu, and Y. P. Sun, J. Mater. Chem. C **4**, 4538 (2016).

[47] J. Xiang, H. Wang, B. Dai, W.-L. Cheng, X.-W. Zhang, Z.-G. Wang, and N.-N. Ge, J. Phys. Chem. Solids **169**, 110834 (2022).

[48] Y.-X. Zhen, M. Yang, H. Zhang, G.-S. Fu, J.-L. Wang, S.-F. Wang, and R.-N. Wang, Sci. Bull. **62**, 1530 (2017).

[49] D. Qin, X.-J. Ge, G.-q. Ding, G.-y. Gao, and J.-T. Lü, RSC Adv. **7**, 47243 (2017).

[50] H. Wang, Y.-S. Lan, B. Dai, X.-W. Zhang, Z.-G. Wang, and N.-N. Ge, ACS Omega **6**, 29820 (2021).

[51] G. Chen, W. Bao, Z. Wang, and D. Tang, Phys. Chem. Chem. Phys. **25**, 9225 (2023).

[52] G. Ding, G. Y. Gao, Z. Huang, W. Zhang, and K. Yao, Nanotechnology **27**, 375703 (2016).

[53] K. Sugawara, Y. Nakata, R. Shimizu, P. Han, T. Hitosugi, T. Sato, and T. Takahashi, ACS Nano **10**, 1341 (2016).

[54] P. Knowles, B. Yang, T. Muramatsu, O. Moulding, J. Buhot, C. J. Sayers, E. Da Como, and S. Friedemann, Phys. Rev. Lett. **124**, 167602 (2020).

[55] K. Dolui and S. Sanvito, Europhys. Lett. **115**, 47001 (2016).

[56] J.-H. Liao, Y.-C. Zhao, Y.-J. Zhao, X.-B. Yang, and Y. Chen, J. Appl. Phys. **127**, 044301 (2020).

[57] J. S. Zhou, L. Monacelli, R. Bianco, I. Errea, F. Mauri, and M. Calandra, Nano Lett. **20**, 4809 (2020).

[58] M. J. Wei, W. J. Lu, R. C. Xiao, H. Y. Lv, P. Tong, W. H. Song, and Y. P. Sun, Phys. Rev. B **96**, 165404 (2017).

[59] B. Singh, C.-H. Hsu, W.-F. Tsai, V. M. Pereira, and H. Lin, Phys. Rev. B **95**, 245136 (2017).

[60] G. Kresse and J. Furthmüller, Phys. Rev. B **54**, 11169 (1996).

[61] J. P. Perdew, K. Burke, and M. Ernzerhof, Phys. Rev. Lett. **77**, 3865 (1996).

[62] See Supplemental Material at http://link.aps.org/supplemental/10.1103/PhysRevB.108.214304 for reliability test of PBE generalized function, convergence test of phonon properties, effect of LO-TO splitting on phonon properties, and comparison of higher-order anharmonicity.

[63] H. Zheng, S. Valtierra, N. Ofori-Opoku, C. Chen, L. Sun, S. Yuan, L. Jiao, K. H. Bevan, and C. Tao, Nano Lett. **18**, 2179 (2018).

[64] S. Karak, J. Bera, S. Paul, S. Sahu, and S. Saha, Phys. Rev. B **104**, 195304 (2021).

[65] A. Shafique, A. Samad, and Y.-H. Shin, Phys. Chem. Chem. Phys. **19**, 20677 (2017).

[66] T. Tadano, Y. Gohda, and S. Tsuneyuki, J. Phys.: Condens. Matter **26**, 225402 (2014).

[67] F. Zhou, W. Nielson, Y. Xia, and V. Ozoliņš, Phys. Rev. B **100**, 184308 (2019).

[68] F. Zhou, B. Sadigh, D. Åberg, Y. Xia, and V. Ozoliņš, Phys. Rev. B **100**, 184309 (2019).

[69] F. Zhou, W. Nielson, Y. Xia, and V. Ozoliņš, Phys. Rev. Lett. **113**, 185501 (2014).

[70] W. Li, J. Carrete, N. A. Katcho, and N. Mingo, Comput. Phys. Commun. **185**, 1747 (2014).

[71] Z. Han, X. Yang, W. Li, T. Feng, and X. Ruan, Comput. Phys. Commun. **270**, 108179 (2022).

[72] S. Jeong, D. Yoo, M. Ahn, P. Miró, T. Heine, and J. Cheon, Nat. Commun. **6**, 5763 (2015).

[73] Z. Zeng, Z. Yin, X. Huang, H. Li, Q. He, G. Lu, F. Boey, and H. Zhang, Angew. Chem. Int. Ed. **50**, 11093 (2011).

[74] M. Zhang, Y. Zhu, X. Wang, Q. Feng, S. Qiao, W. Wen, Y. Chen, M. Cui, J. Zhang, C. Cai, and L. Xie, J. Am. Chem. Soc. **137**, 7051 (2015).

[75] Y. Cao, T. Wähler, H. Park, J. Will, A. Prihoda, N. Moses Badlyan, L. Fromm, T. Yokosawa, B. Wang, D. M. Guldi *et al.*, Adv. Mater. Interfaces **7**, 2001493 (2020).

[76] K. Xu, Z. Wang, F. Wang, Y. Huang, F. Wang, L. Yin, C. Jiang, and J. He, Adv. Mater. **27**, 7881 (2015).

[77] R. Yue, A. T. Barton, H. Zhu, A. Azcatl, L. F. Pena, J. Wang, X. Peng, N. Lu, L. Cheng, R. Addou *et al.*, ACS Nano **9**, 474 (2015).

[78] R. M. Badger, J. Chem. Phys. **2**, 128 (2004).

[79] R. M. Badger, J. Chem. Phys. **3**, 710 (2004).

[80] I. D. Brown and R. D. Shannon, Acta Crystallogr. Sect. A **29**, 266 (1973).

[81] W. Gordy, J. Chem. Phys. **15**, 305 (2004).

[82] H. Qi, Z. Sun, C. Shen, Z. Chang, Z. Wang, X. Wang, M. Zhang, and N. Wang, ACS Appl. Energy Mater. **5**, 7371 (2022).

[83] S. Maintz, V. L. Deringer, A. L. Tchougréeff, and R. Dronskowski, J. Comput. Chem. **37**, 1030 (2016).

[84] T. Wang, Y. Xiong, Y. Wang, P. Qiu, Q. Song, K. Zhao, J. Yang, J. Xiao, X. Shi, and L. Chen, Mater. Today Phys. **12**, 100180 (2020).

[85] J. He, Y. Xia, W. Lin, K. Pal, Y. Zhu, M. G. Kanatzidis, and C. Wolverton, Adv. Funct. Mater. **32**, 2108532 (2022).

[86] K. Pal, Y. Xia, J. He, and C. Wolverton, Phys. Rev. Mater. **3**, 085402 (2019).

[87] J. P. Heremans, Nat. Phys. **11**, 990 (2015).

[88] T. Li, P.-H. Du, L. Bai, Q. Sun, and P. Jena, Phys. Rev. Mater. **6**, 064009 (2022).

[89] Y. Xiao, C. Chang, Y. Pei, D. Wu, K. Peng, X. Zhou, S. Gong, J. He, Y. Zhang, Z. Zeng, and L.-D. Zhao, Phys. Rev. B **94**, 125203 (2016).

[90] S.-Y. Yue, G. Qin, X. Zhang, X. Sheng, G. Su, and M. Hu, Phys. Rev. B **95**, 085207 (2017).

[91] S. Bi, Z. Chang, K. Yuan, Z. Sun, X. Zhang, Y. Gao, and D. Tang, J. Appl. Phys. **132**, 114301 (2022).

[92] L. Yu, A. Chen, X. Wang, H. Wang, Z. Qin, and G. Qin, Phys. Rev. B **106**, 125410 (2022).

[93] H. Wang, C. Gao, B. Peng, J. Wu, X. Wang, D. Wei, L. Tan, Z. Qin, and G. Qin, Nanotechnology **34**, 175704 (2023).